Design of an Airborne L-band Cross-track Scanning Scatterometer

Final Report

September 18, 2002

Prepared for:

NASA Goddard Space Flight Center
Grants Office
Code 210.G
Greenbelt, MD 20771-0001

NASA Technical Point of Contact:

Lawrence M. Hilliard
Mail stop 410.0
Greenbelt, MD 20771

Submitted by:

ProSensing Inc.
107 Sunderland Road
Amherst, MA 01002-1098, USA

1. Abstract

In this report, we describe the design of an airborne L-band cross-track scanning scatterometer suitable for airborne operation aboard the NASA P-3 aircraft. The scatterometer is being designed for joint operation with existing L-band radiometers developed by NASA for soil moisture and ocean salinity remote sensing. In addition, design tradeoffs for a space-based radar system have been considered, with particular attention given to antenna architectures suitable for sharing the antenna between the radar and radiometer.

During this study, we investigated a number of imaging techniques, including the use of real and synthetic aperture processing in both the along track and cross-track dimensions. The architecture selected will permit a variety of beamforming algorithms to be implemented, although real aperture processing, with hardware beamforming, provides better sidelobe suppression than synthetic array processing and superior signal-to-noise performance.

In our discussions with the staff of NASA GSFC, we arrived at an architecture that employs complete transmit/receive modules for each subarray. Amplitude and phase control at each of the transmit modules will allow a low-sidelobe transmit pattern to be generated over scan angles of +/-50 degrees. Each receiver module will include all electronics necessary to downconvert the received signal to an IF offset of 30 MHz where it will be digitized for further processing.

2. Introduction

This report describes design options for an L-band cross-track scanning scatterometer to compliment 1D- and 2D-ESTAR, existing imaging radiometers developed by NASA GSFC in cooperation with the University of Massachusetts and ProSensing Inc. The long term goal of this project is to develop a radar/radiometer system that will employ a single broadband antenna that can support simultaneous radar and radiometric measurements from an airborne or space based platform. Key constraints set forth at the outset of the study are listed below.

- The scatterometer should be designed for joint operations with ESTAR or another cross-track scanning radiometer with joint use of the data from the two instruments.
- The scatterometer will use an antenna that is substantially similar to the ESTAR antenna, at least for the scatterometer's receiving antenna, if a separate transmit antenna is used.
- The system will employ cross-track scanning with multiple beam positions, possibly with a cross-track steering resolution of about ½ the beam width (nominally about 15°), and with beam positions out to an incidence angle of ~45-50 degrees.
- There should be a reasonably good matching between the scatterometer and ESTAR beam positions and beam shapes. The beam positions should be as close to identical as is practical, so the scatterometer and ESTAR data can be assumed to come from the very nearly the same geophysical target.
- Flight operation is planned on the NASA P-3 aircraft, which flies at a true airspeed of about 130 m/s, and at altitudes between 0.5 and 8 km, msl.
- Doppler beam sharpening is NOT planned for an initial instrument.
- The scatterometer must be able to observe typical Earth surface backscatter at the typical aircraft flight altitudes, and when the integration period is no longer than ½ the time it takes the aircraft to traverse one beam footprint on the Earth surface.

After the study got underway, NASA requested that we also consider design concepts for a spaced-based version of the system that would use—as much as possible—common antenna and RF hardware for the radar and radiometer. Design of an airborne radar/radiometer with shared hardware is also being investigated.

3. Antenna and Beamforming Design Considerations

Conceptual diagrams of the various radar system configurations are shown in Figures 1 and 2. Two methods of distributing the signal from a conventional radar are shown in Figure 1. The first uses a conventional beamforming network consisting of a means of power division and independently controllable phase shifters for each element in the antenna array. Conventional beamforming generates a focused antenna beam pattern on transmit and receive. The second method employs a 1:N switch to steer the radar to a specific element in the array, with switching from element to element at the radar pulse repetition frequency. This approach allows synthetic generation of the antenna pattern with arbitrary pointing angle and arbitrary amplitude taper, both determined by post processing. Figure 2 shows an alternate architecture, where each element in the array is connected to an independent transmit/receive module, with arbitrary control of the transmitter's amplitude and phase and a digital receiver incorporated in each module, that stores I/Q pairs versus range for each receiver. Although this architecture has the highest complexity, it also offers the greatest flexibility for beam generation and signal processing. For a variety of reasons this approach appears the most suitable for the present investigation. These reasons include the relatively low cost of RF electronics at L-band, the small number of subarrays in the airborne antenna, and the ease of implementing a digital receiver for the proposed system, which should require no more than a few MHz of video bandwidth per receiver. For these reasons, the rest of this report will focus on issues pertaining to the architecture shown in Figure 2.
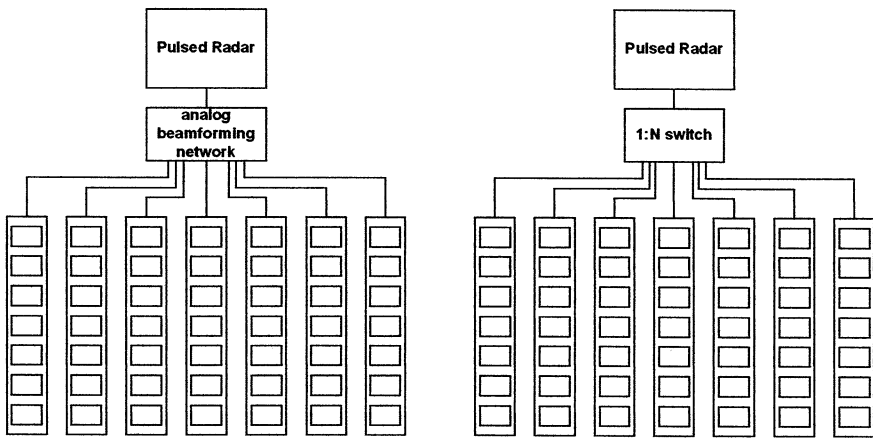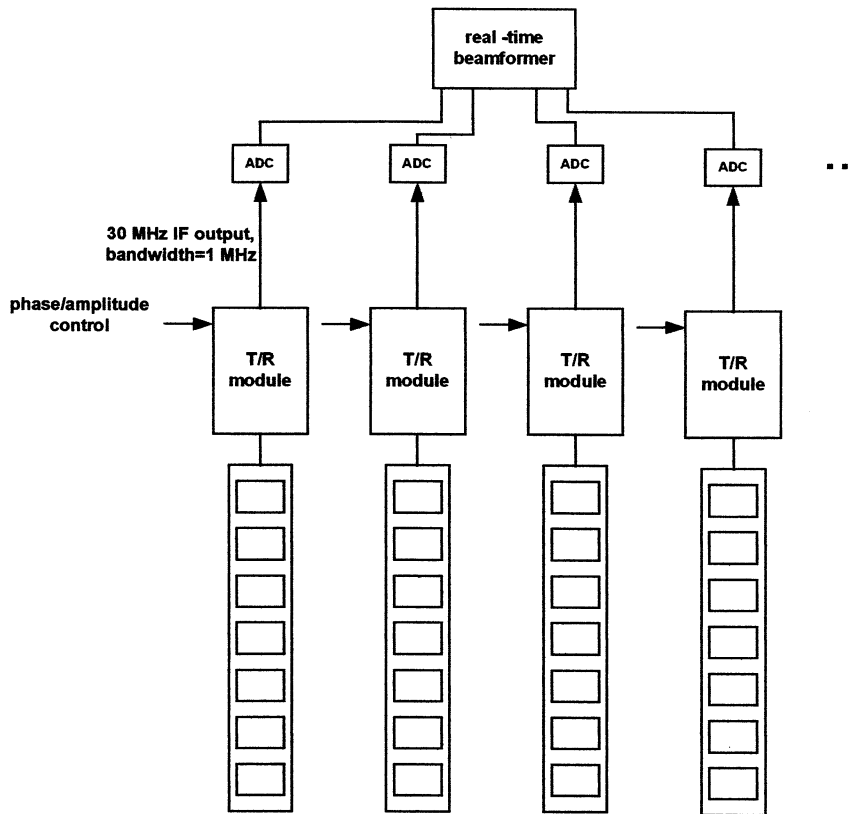

Figure 1 Single channel radar, with analog beamforming or 1:N switch.

Figure 2. Distributed radar with individual t/r modules.

Beamforming Approaches

There are several beamforming options available when using the system architecture shown in Figure 2. These are

1. Simultaneous transmission and reception on all subarrays.

2. Transmission on a single subarray, simultaneous reception on all subarrays.

3. Sequential transmission and reception on each subarray.

Each of these methods of beamforming has unique strengths and weaknesses, as summarized in the following paragraphs.

Case 1: Simultaneous Transmission and Reception on all Subarrays

Transmitting and receiving simultaneously on all of the subarrays is the typical operating mode for conventional phased array radars. This allows a focused beam to be formed on transmission, with amplitude tapering and beam steering achieved by adjusting the gain and phase of the individual transmit modules. Similar amplitude and phase tapering can be applied to the digitized signal to steer the received beam and control its sidelobe structure. The two-way gain for this array is given by the product of the transmit and receive array factor and element factor:

$$G(\theta) = \left| \sum_{i=0}^{N-1} A_i^t E(\theta) e^{jikd\sin\theta_i} \right|^2 \times \left| \sum_{i=0}^{N-1} A_i^r E(\theta) e^{jikd\sin\theta_r} \right|^2 ,$$

where $k = 2\pi / \lambda$, d is the spacing between the N subarrays, $A_i^{t,r}$ is the relative weighting (voltage) of each subarray on transmit and receive, $E(\theta)$ is the subarray voltage gain factor, and $\theta_{t,r}$ is the scan angle of the beam peak measured from broadside for the transmit and receive arrays (typically, $\theta_r = \theta_t$).

If identical amplitude and phase tapering are employed on transmit and receive, the two way power gain is given by

$$G(\theta) = \left| \sum_{i=0}^{N-1} A_i \, E(\theta) e^{jikd\sin\theta} \right|^4 .$$

Practical two-way sidelobe levels for such an array can approach 50 dB, since the sidelobes are determined by the product of the transmit and receive levels, which will be around 25 dB for a practical antenna of this size. Other advantages of Case 1 include the fact that all of the t/r units are used together, resulting in an increase in average power by a factor equal to the number of subarrays. For the case of a radar with ten subarrays, this will yield a 10 dB improvement in sensitivity or a factor of ten reduction in the required peak transmit power per module.

Case 2: Transmission on a Single Subarray, Reception on all Subarrays

In this case, the central subarray is energized, illuminating the entire field of view on each pulse of the radar. The signals received at all of the subarrays are sampled, then a digital beamforming algorithm is executed which forms simultaneous beams at various scan angles. The two way gain for this array is given by:

$$G(\theta) = |E(\theta)|^2 \left| \sum_{i=0}^{N-1} A_i^r E(\theta) e^{jikd \sin\theta_r} \right|^2 .$$

For a given amplitude taper, Case 2 is seen to have sidelobes which are twice that of Case 1, so the practical sidelobe level will be around 25 dB. The primary advantage of this type of beamforming is that it provides simultaneous imaging on all beams, which is advantageous when observing scenes that are rapidly evolving in time.

Case 3: Sequential Transmission and Reception on Individual Subarrays

Transmitting and receiving sequentially on individual subarrays will yield an across-track pattern with properties identical to that of a synthetic aperture radar. The primary advantage of this beamforming method is that sequential sampling yields a reduction in the 2-way beamwidth by a factor of $\sqrt{2}$ compared to Case 1 and by a factor of two compared to Case 2. The two-way gain factor for Case 3 is given by
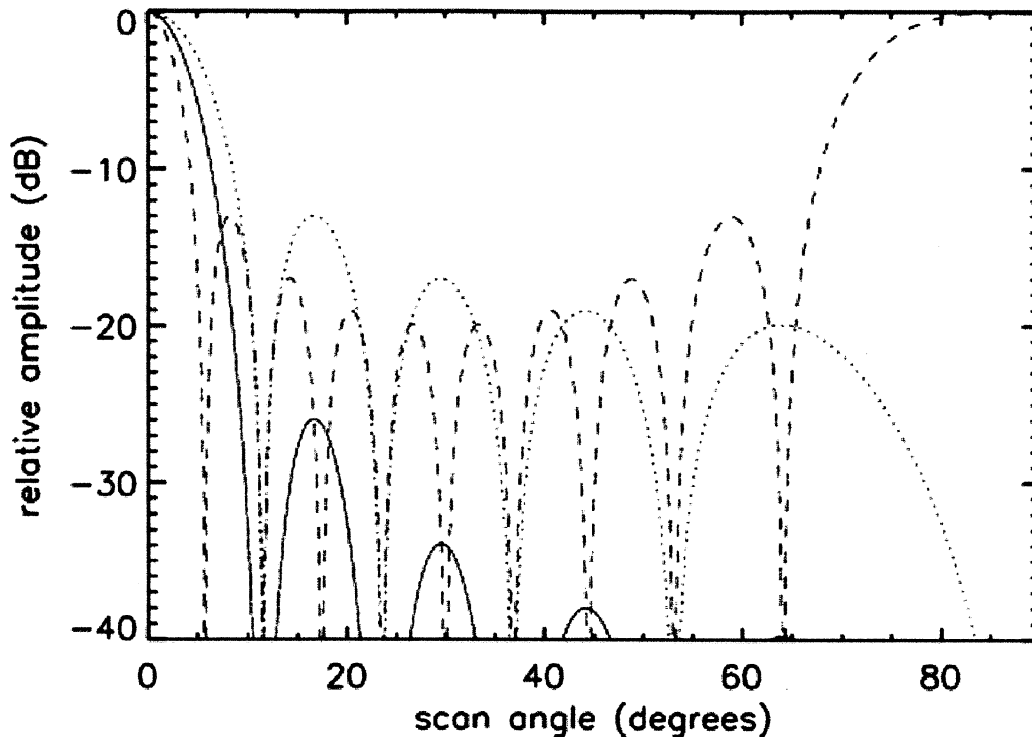
$$G(\theta) = \left| \sum_{i=0}^{N-1} A_i^t A_i^r E^2(\theta) e^{2jikd \sin\theta_t} \right|^2 .$$

This expression shows that the array factor for Case 3 is similar to that of a receive-only array (Case 2) operating at twice the frequency, although amplitude tapering can be applied twice (on transmit and receive). Practical sidelobe levels for such an array should be around 25 dB.

Conventional SAR processing requires that the synthetic array be sampled at $D/2$, where D is the along-track length of the real aperture. Sampling a real or synthetic aperture a spacing greater than $D/2$ results in grating lobes, the equivalent of Doppler aliasing in SAR. In this case, the subarrays are spaced at half wavelength intervals. This spacing leads to grating lobes spaced at unit intervals in $u = \sin(\theta)$ space. When pointing broadside (u=0), grating lobes will also be generated at +/- 90 degrees (u=+/-1). When scanning to +30 degrees (u=.5), an equal gain beam will be generated at –30 degrees (u=-.5). Scanning at other angles (say 0 to 25 degrees, and beyond 35 degrees) may be practical if the grating lobe can be range-gated out of the image, but range gating cannot separate the –30 and +30 degree beams.

Two-way gain patterns for all three cases are plotted in Figure 3, assuming a uniform amplitude taper and isotropic element factor. The beamwidths for cases 1, 2 and 3 are 10.2, 13.9 and 6.95 degrees, respectively.

Figure 3 Two-way power gain of beamforming Case 1 (solid line), 2 (dotted line), and 3 (dashed line). Assumption: uniform amplitude taper, 10 elements, spaced one-half wavelength at 1.26 GHz, no element factor.

For all cases, storage of the raw digitized radar output will allow post-processing of the beams, allowing various amplitude and phase tapers to be applied to achieve optimal pattern control. For example, if an interfering source is present on the ground, a pattern null can be placed at the angle of the interfering signal to reduce contamination of the desired signal. This pattern null can be applied to the receive array factor for Cases 1 and 2, and to the combined array factor for Case 3.

A summary of the strengths and weaknesses of Cases 1-3 is provided in Table 1. Case 1 appears to be superior for the present application, given that it combines excellent sidelobe control with the best utilization of transmit power. However, since all three methods can be implemented without additional hardware costs it may be worthwhile to configure the system to operate in all three modes for the demonstration system.

Table 1. Summary of beamforming options.

	Case 1	Case 2	Case 3
Description	Simultaneous t/r on all subarrays	Central subarray tx, simultaneous rx on all subarrays	Sequential t/r on individual subarrays
Advantages	Highest gain, lowest sidelobes, lowest required tx power per module	Pulse to pulse imaging on all beams	Narrowest beamwidth
Disadvantages	No significant disadvantages	Widest beamwidth, poor sidelobe control	Poor sidelobe control, grating lobes issues

Microstrip Antenna

Single Frequency Operation

The antenna subarray selected for the first airborne scatterometer will be a corporate fed microstrip patch array of eight patch elements. Ten of these subarrays will make up the overall antenna, with the central eight active, and the outer two subarrays terminated in a matched load to reduce the effects of uneven mutual coupling. Dual polarized patches with good mutual coupling properties and good polarization isolation have been developed for ESTAR-2D at 1.415 GHz. These patches, shown in Figure 4 can be scaled from 1.415 to 1.26 GHz and can employ a corporate feed system similar to one developed at our company for a salinity mapping radiometer, as shown in Figure 5. A provision will be made for separate corporate feeds for vertical and horizontal polarization, although only one feed will be built to reduce the cost of the first airborne system. Table 2 summarizes the important features of the overall antenna.

Table 2. Antenna parameters.

| Parameter	Description
Antenna Type	Microstrip Patch Array (10 subarrays of 8 elements/subarray)
Frequency	1.26 GHz
Bandwidth (10 dB return loss)	18 MHz
Polarization	Horizontal
3 dB Beamwidth (Nadir, along track)	15+/- 1 Degrees
Subarray gain	≥ 10.5 dB
Side Lobes	Better than -18 dB
Scan Angle Range	± 50 degrees

Dual Frequency Operation

In future airborne and spaceborne systems, it may be desirable to use a single, broadband antenna for both the radar and radiometer. In order to operate simultaneously at 1.26 GHz (scatterometer) and 1.415 GHz (radiometer), the individual radiating elements will need to be modified to a wideband patch using well known techniques [D.M. Pozar, *A review of bandwidth enhancement techniques for microstrip antennas*, in Microstrip Antennas, D.M.Pozar, D.H. Schaubert, eds., IEEE Press, 1995, pg. 157-166.]. Broadband techniques will be required if the radar is to share an antenna with a thinned array L-band radiometer, such as 1D or 2D STAR. For the present application, a bandwidth of approximately 13% is required. This can be achieved by using aperture coupling between the feed network and the patch, and by using a relatively thick (0.5 cm) low dielectric constant substrate [[D.M. Pozar and B. Kaufman, *Increasing the bandwidth of a microstrip antenna by proximity coupling*,in Microstrip Antennas, D.M.Pozar, D.H. Schaubert, eds., IEEE Press, 1995, pg. 178-179].

Figure 4. Dual polarized microstrip patch array printed on .125" thick Teflon-fiberglass substrate.
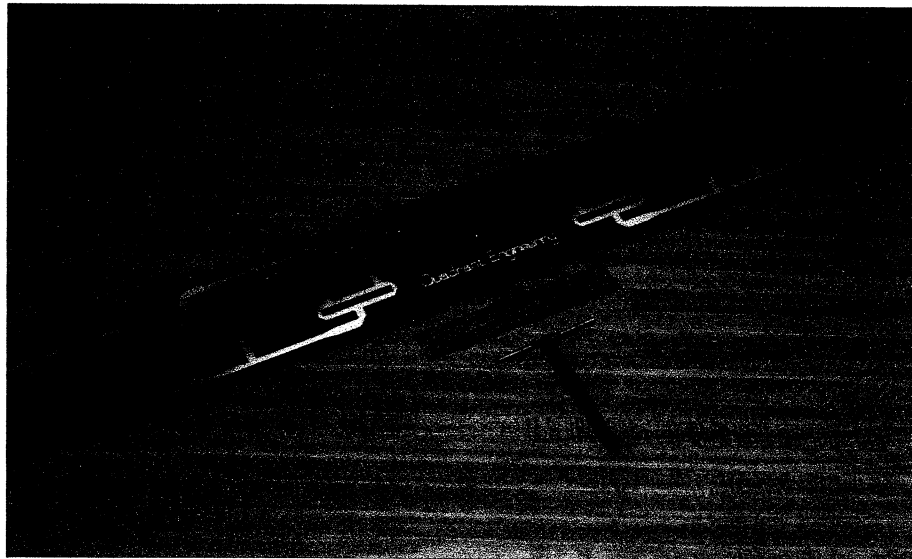
Figure 5. 1.415 GHz in-phase corporate feed network.

Scan Blindness

One potential problem with all phased array antennas is a phenomenon called scan blindness. Mutual coupling between closely spaced array elements changes as a function of scan angle. For large scan angles, typically greater than 30 degrees off broadside, the input reflection coefficient of each element in the array will equal 1.0, reflecting the input signal on transmit, and scattering all incident power on receive. Scan blindness has been investigated for large phased array radar using waveguide and dipole elements [L. Stark, "Microwave Theory of Phased-Array Antennas-A Review", Proc. IEEE, 62(12), Dec. 1974, 1661-1701] and for microstrip arrays [D. M. Pozar and D. H. Schaubert, "Scan Blindness in Infinite Phased Arrays of Printed Dipoles," IEEE Trans. Antennas and Propagation, Vol. AP-32, pp. 602-610, June 1984]. Scan blindness angles differ for the E-plane and H-plane scanning, meaning that there may be a blindness problem for one or both polarizations.

D.M. Pozar has determined the blindness angle using the program PCAAD for an infinite array of microstrip patches spaced .1185 m apart (half wavelength at 1.26 GHz), for a substrate thickness of .125" and relative dielectric constant of 2.2. Under these conditions, there is no blindness angle at 1.26 GHz. Dr. Pozar also looked at scan blindness for a shared radar/radiometer antenna using the criteria that the elements or subarrays are spaced one-half wavelength at 1.26 GHz and .56 wavelengths at 1.415 GHz. For this
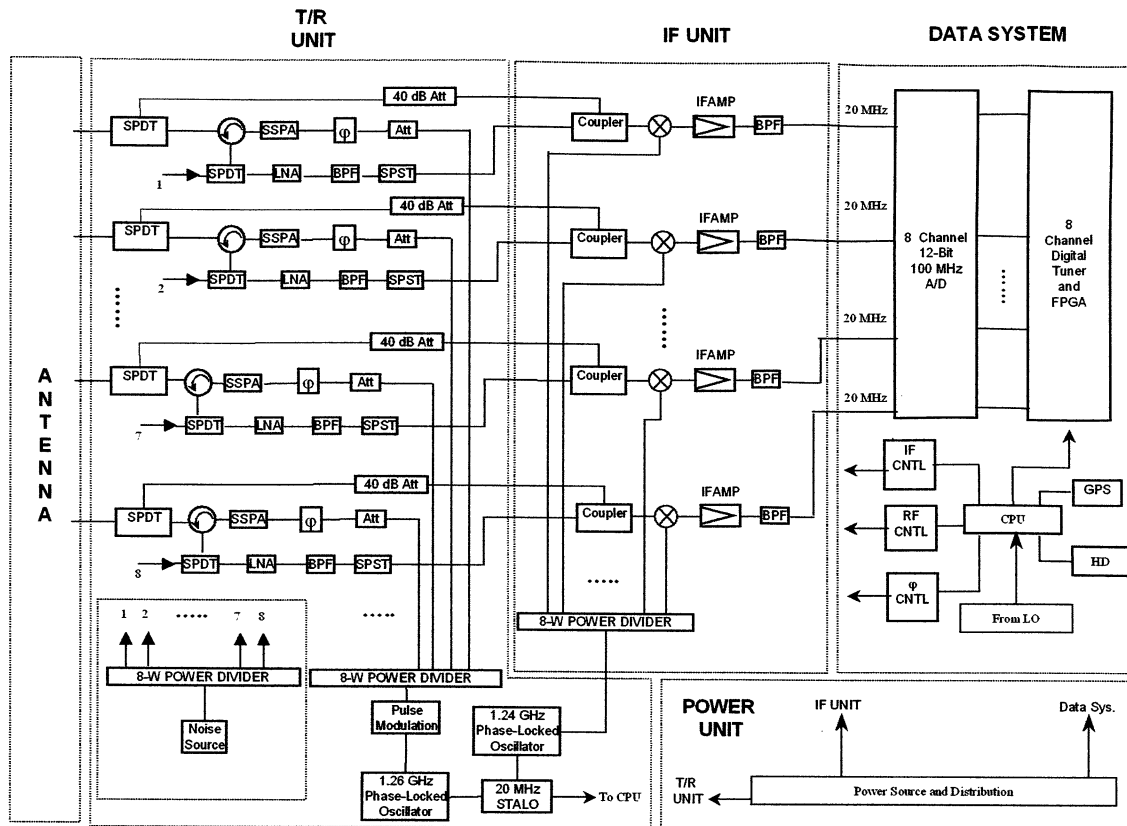
configuration, scan blindness occurs at 1.415 GHz for a scan angle of 51 degrees when scanning in the E-plane (cross-track scanning, vertical polarization). Array performance will significantly degrade for scan angles within 10 or 15 degrees of the blindness angle, limiting E-plane scans at 1.415 GHz to 36-41 degrees for this element or subarray spacing. This presents a problem for the radiometric channel of a combined radar/radiometer, since the spec calls for scanning out to 50 degrees.

The solution to this problem is to reduce the array spacing so that it falls closer to $\lambda/2$ at 1.415 GHz and below $\lambda/2$ at 1.26 GHz. We have been working under the assumption that this tight spacing would cause a mutual coupling problem at 1.26 GHz. While this may be the case for a microstrip patch, it may not be a major problem for other element designs such as a printed dipole.

4. Radar RF Design

A detailed block diagram of the radar system, prepared by NASA GSFC, is shown in Figure 6. The system includes a common phase-locked reference that is phase shifted independently on each channel before amplification and transmission. The received signals are downconverted using a common phase-locked local oscillator, offset from the transmit PLO by the IF frequency of 20 MHz. The IF signals are digitized at a rate of approximately 100 MS/s, using a 12-bit ADC. After digital filtering is applied, the effective dynamic range should be greater than 75 dB, sufficient to account for variations in signal level without the use of an AGC or RTC circuit.
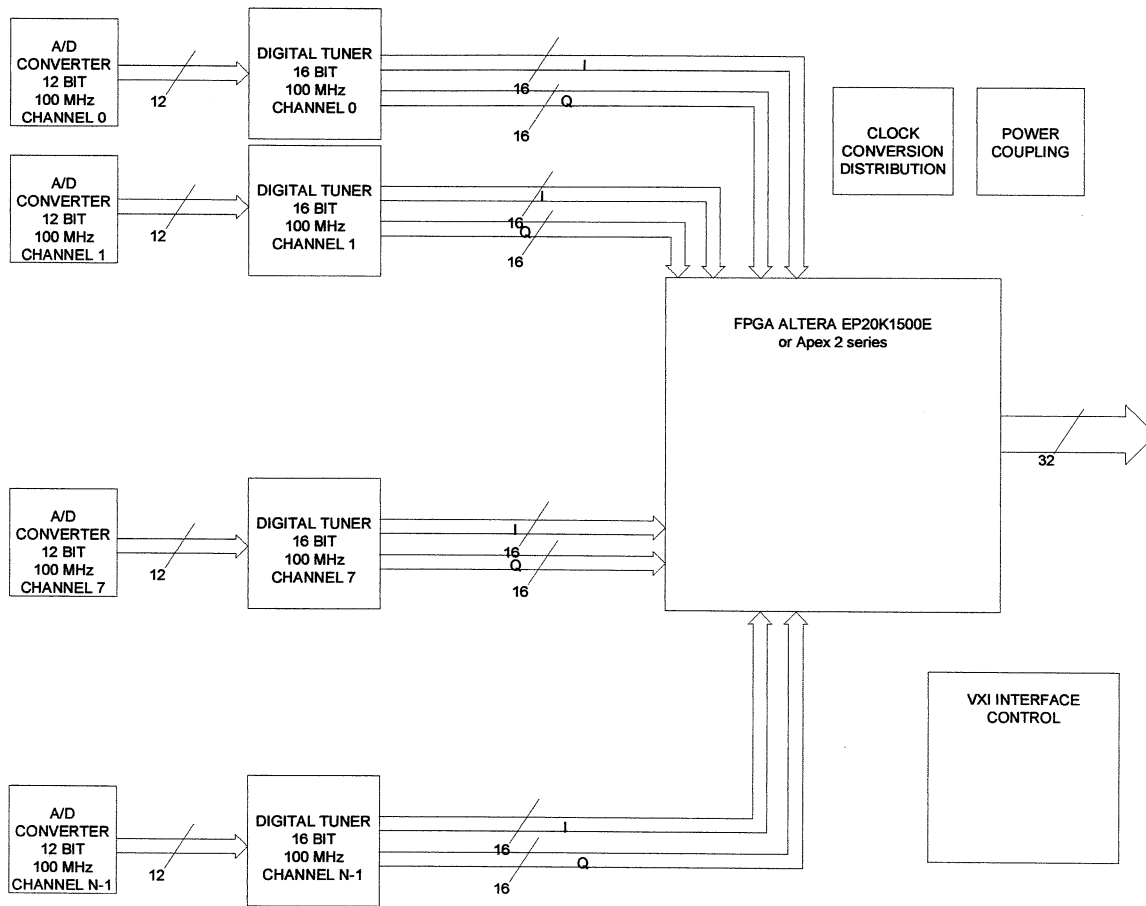
Figure 6 Block diagram of prototype radar system.

Digital receiver/signal processor

The digital receiver/signal processor required by the L-band radar will include a 100 MS/s digitizer, followed by a ASIC digital I/Q detector, followed by a high performance FPGA processor for beam forming. A block diagram of the digital receiver/signal processor is shown in Figure 7. The digital beam former will perform conventional beam synthesis on receive for up to 20 range gates. A raw data storage mode will also be implemented, allowing synthetic generation of the antenna pattern with arbitrary pointing angle and arbitrary amplitude taper, both determined by post processing.
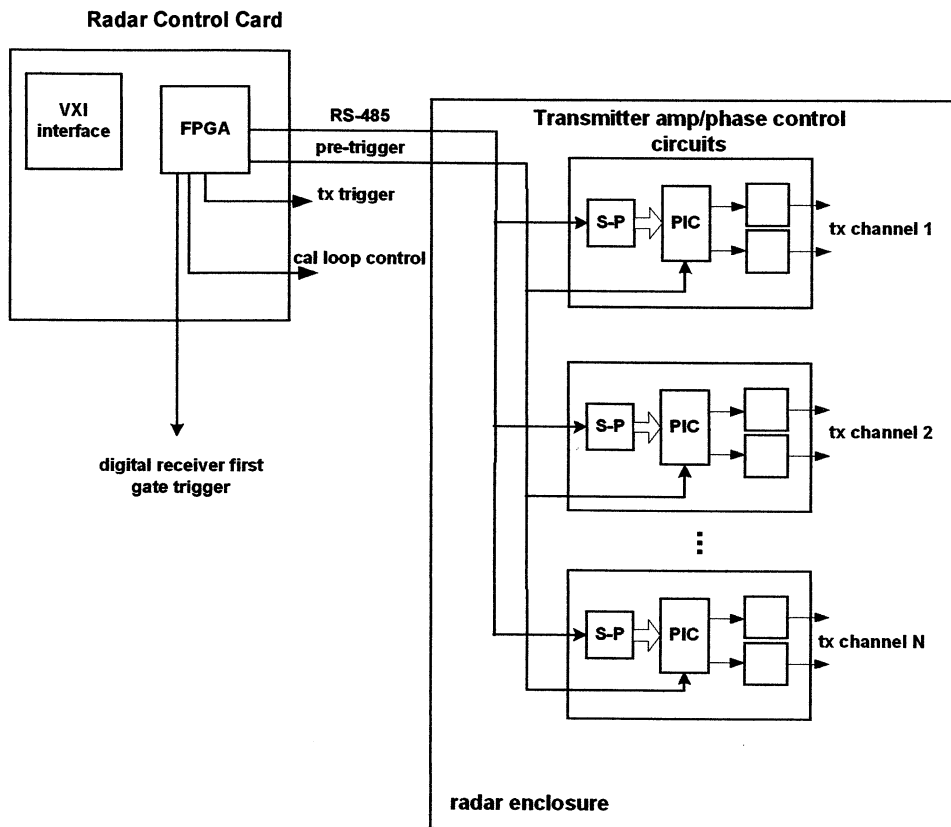
Figure 7. Digital receiver/signal processor block diagram.

Beam Steering Controller Cards

The radar will include beam steering control circuits to provide the necessary amplitude and phase adjustment of the control voltage at each of the antenna subarrays in order to obtain a proper taper across the antenna elements as well as fast cross-track scanning. All circuits will be fully documented with schematics and component specifications. A block diagram of the proposed radar control circuit is shown in Figure 8.

Radar Control Card

Figure 8. Radar control card with amplitude and phase control drivers for each subarray.

5. Spaceborne Radar Antenna Design Considerations

The challenge of operation from space is to find some means of sharing as much antenna hardware as possible between the radar and radiometer. For this study, we have assumed that the spaceborne radiometer will employ some form of two-dimensional thinning, while the radar will use SAR processing to achieve the desired resolution. It may be possible to use ESTAR-like processing for radar imaging, using a flood beam for transmission and the 2D thinned array with correlation processing on receive. Determining the effectiveness of correlation processing for radar imaging is beyond the scope of the current study.

A good review of the design considerations for spaceborne SAR is provided in [Ulaby, Moore, and Fung, 'Microwave Remote Sensing, Active and Passive, Volume II, Artech House, 1982, chapter 9]. The high ground-speed of low-earth orbiting satellites

(approximately 7500 m/s) and the large extent of the cross-track range swath (hundreds of kilometers) place competing constraints on the required radar pulse repetition frequency to avoid Doppler aliasing and range ambiguities. This results in a constraint on the area of the radar antenna, given in terms of average target range, R_{av}, the space craft velocity, u, the average incidence angle, θ_{av}, and the frequency, f:

$$area_{min} = \frac{4KuR_{av}\tan(\theta_{av})}{f}$$

where $K \approx 3.2$ is a constant depending on the antenna taper and bandpass safety factors.

If the cross-track length of the antenna is fixed by other considerations, this formula can be solved for the minimum length of the subarray in the along track direction, L_y:

$$L_y = \frac{4KuR_{av}\tan(\theta_{av})}{fL_x}$$

For example, one of the proposed space based radiometer configurations is to use a pair of 14.1 m x14.1 m 1D-thinned arrays for the radiometer. A radar antenna might be interleaved with the radiometer, as shown in Figure 9, with the radar cross-track length limited to 14.1 m to fit in the same footprint as the radiometer antenna. Minimum along-track subarray length is plotted in Figure 10 as a function of scan angle. This figure shows that the radar antenna would have to be 7.3 m long, still substantially smaller than the radiometer.

The analysis above shows that a standard L-band SAR would require an antenna 14.1 m x 7.3 m in area to avoid ambiguous range and Doppler problems while scanning out to just beyond 50 degrees. A radar antenna of this size would consist of 120 subarrays, spaced at $\lambda/2$ ($\lambda = .2337m$), with each subarray consisting of 64 patches, also spaced at $\lambda/2$. This antenna could provide a cross-track swath width of 10 km if the antenna aperture were uniformly illuminated (leading to 13 dB one-way sidelobes). These sidelobes can be removed by range gating, and would therefore not pose a problem.

Interleaving the two antennas can be accomplished several ways. These include:

- The radar and radiometer could share a common radiating element at the overlap points.

- The radar antenna could be thinned, removing subarrays where the radiometer subarrays are located. This thinning factor would be about 10 percent, leading to
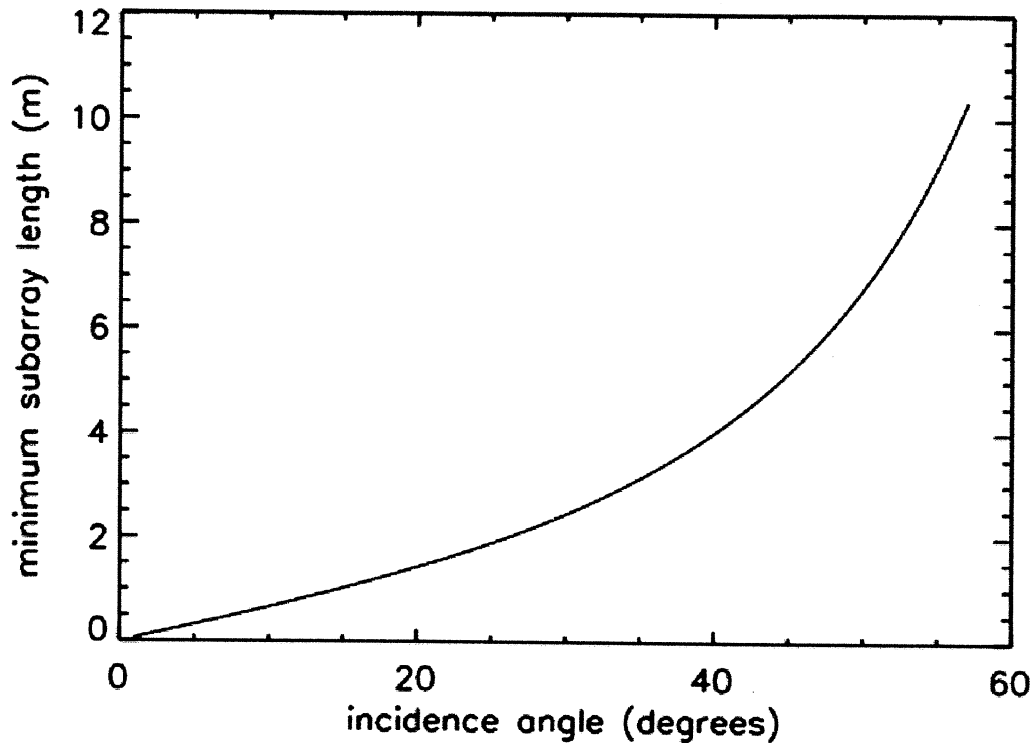
some degradation in sidelobe control. This may not be a big problem, since sidelobes energy can be removed by range gating.

14.1 X 14.1 METER PATCH ANTENNA

UNITS ARE IN MILLIMETERS
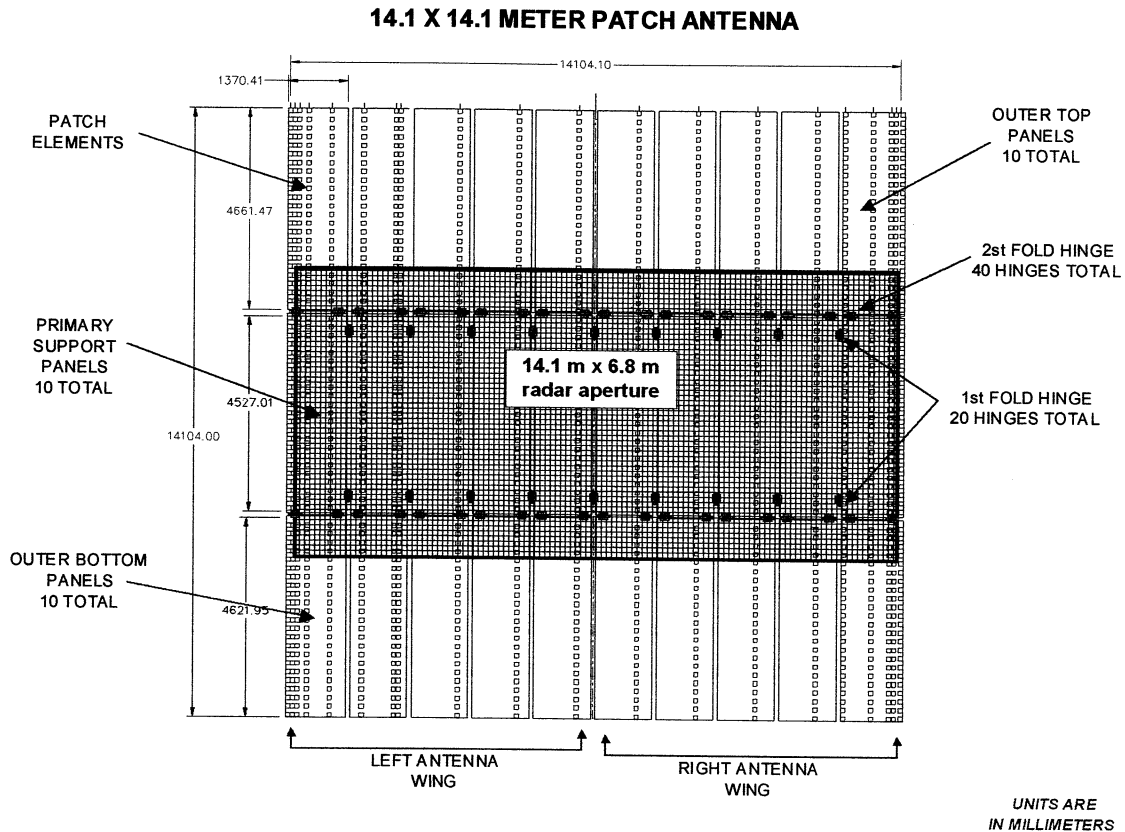
Figure 9 1-D satellite-based thinned array radiometer antenna (in red) with embedded digital beamforming radar antenna (in black).

Figure 10 Minimum subarray length versus scan angle for spaceborne SAR required to avoid Doppler aliasing.

One way to reduce the size of the antenna is to come up with some method to operate at a higher PRF that avoids the ambiguous range problem associated with standard pulsing methods. One obvious idea is to use some sort of pulse coding that allows backscatter from adjacent pulses in time to be separated with sufficient isolation to separate ambiguous returns. For example, a linear-FM up-chirp could be transmitted on even pulses while odd pulses employ a linear-FM down-chirp. All of the codes used in such a scheme would need to have similar power spectra in order that compressed pulses associated with different codes are highly correlated with one another. This is necessary to maintain coherence for Doppler beam sharpening. If N codes are used on N successive pulses, the PRF can increase by a factor of N, and the along track length of the antenna can be reduced by a factor of N. It is not known whether N can be larger than two for a practical system.

Simultaneous processing of two signals with unique codes can be handled as follows. Using the example of linear FM chirps (N=2), the signal can be digitized as before, followed by two beamforming algorithms, one preceded by a matched filter for the up-

chirp, and one with a matched filter for the down-chirp. After filtering, the signals can be processed in the usual way.

6. Software Simulation of Ocean Surface Imaging

Simulation software developed under a DARPA-funded SBIR has been modified to test the imaging radar architectures described in this report. The code has been modified to image using the Case 2 and Case 3 architectures, and will soon be modified to handle Case 1 imaging. The software has also been modified to simulate ocean scenes using the NRCS versus angle profiles provided by S. Velichko and reproduced in Figure 11.
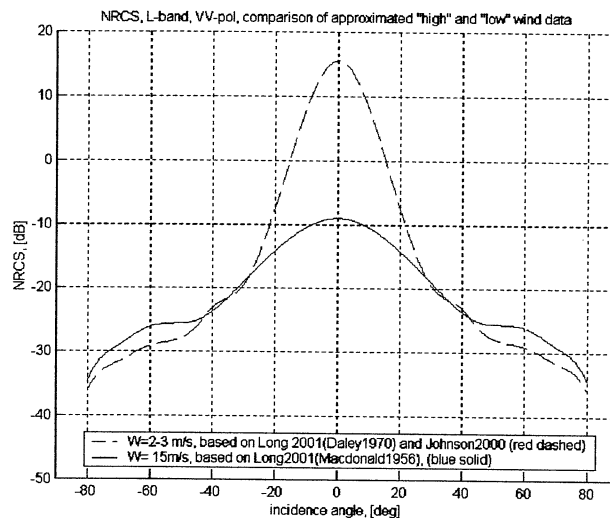
Figure 11 NRCS vs. incidence angle for low and high wind speeds at VV polarization.

Examples of the simulated response of the ocean surface for Case 1, Case 2 and Case 3 imaging are shown in Figure 12 under low wind conditions, from a height of 8 km. The ideal variation in NRCS, based on the model, is shown as a dotted line for comparison. Case 1 beamforming—seen at the top—gives good reproduction of the NRCS profile, with some deviation due to the limited number of independent samples (five) and the relatively broad beamwidth.

Case 2 and Case 3 are seen to yield poorer NRCS profiles. For Case 2, the poor tracking of the NRCS profile at large cross-ranges (near 6-8 km) is due to the fact that the 10 element array has average sidelobe levels on the order of –25 dB. Also, the beamwidth for

Case 2 is the broadest of the three cases, leading to smearing of the NRCS profile near nadir. Case 3, does an excellent job of tracking the profile near nadir. However, the effects of the grating lobes located 90 degrees from the pointing angle of the main beam are seen with a large rise in measured cross-section for large scan angles. The grating lobe can be completely eliminated by range gating, except at angles near 45 degrees.

Imaging simulated scenes

The simulation software can also be used to simulate the response of a simulated scene to the radar using various beamforming cases. To show the capability of the software, we began with an aerial photograph of Logan Airport and Boston Harbor, shown in Figure 13. Land masses were converted to a fixed NRCS of -10 dB m^2/m^2, the water surface was assumed to fit the low wind (3 m/s) model shown in Figure 11, and hard targets, such as ships and the bridge were given a fixed NRCS of $+10$ dB m^2/m^2. Making these assumptions, we created an ideal 1200-look image of the scene, as shown in Figure 14 having a pixel size of 246 m x 246 m.
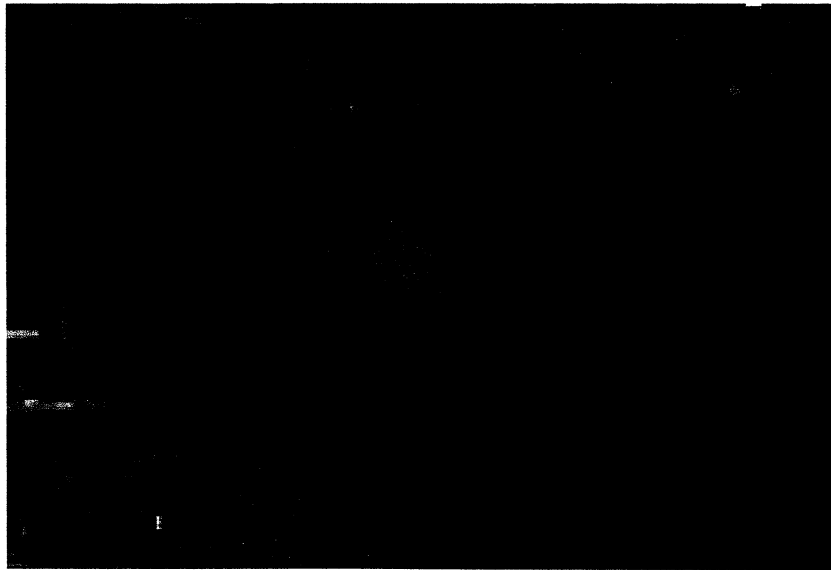
A high resolution pushbroom image of this scene, shown in Figure 15, was generated using an L-band radar having 32 subarrays spaced at $\lambda/2$, with each subarray 4.4 m in length. The radar footprint was 449 feet cross-track x 696 feet along-track as measured by the impulse response of a point scatterer. This figure shows that a large aperture radar can do a good job at reproducing an ideal NRCS image having gross feature similar to that shown in Figure 14.
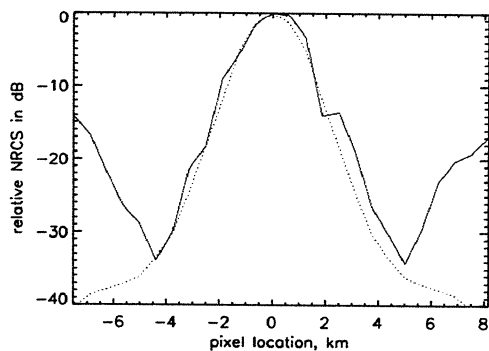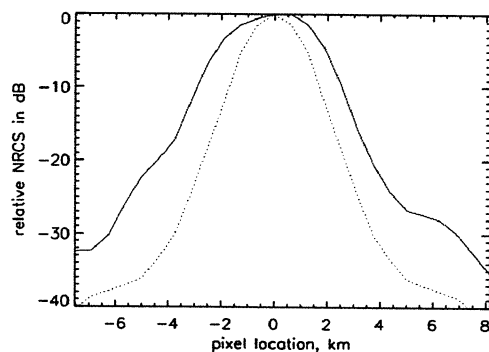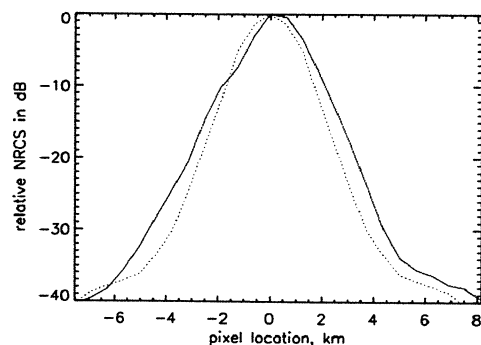
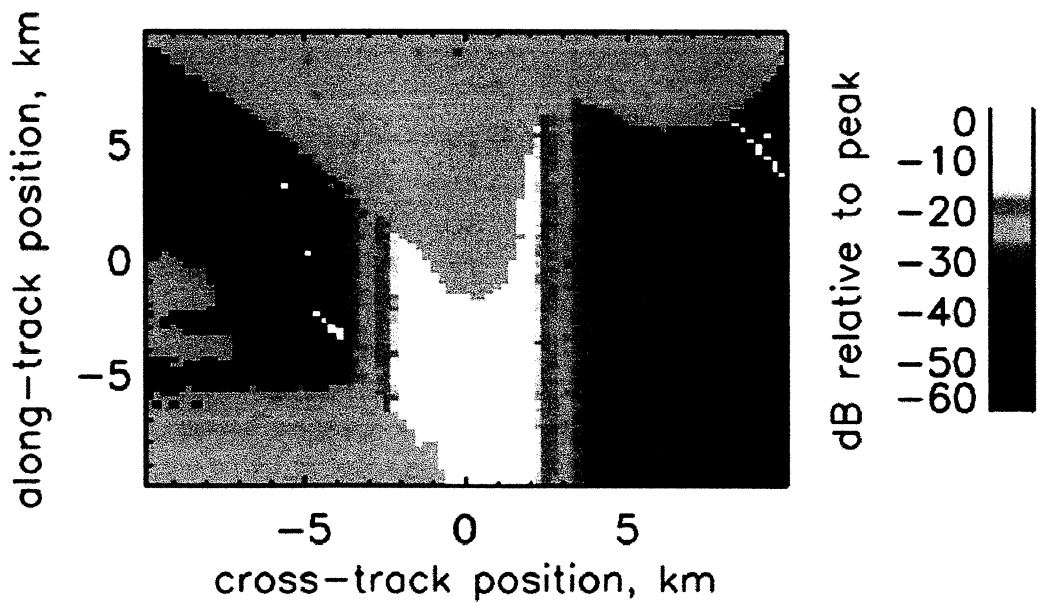Figure 12 Cross track profile of low wind speed NRCS derived by simulated radar return from the ocean surface (solid line) with actual profile shown for comparison (dotted line). Top: Case 1 beamforming; Middle: Case 2 beamforming; Bottom: Case 3 beamforming; All cases, 10 subarrays, 5 look processing, cosine taper with .2 pedestal.

Figure 13 Aerial photograph of Logan Airport and Boston Harbor.

Figure 14. Ideal 1200-look NRCS scene of 81x81 pixels. Note specular flash from smooth ocean at nadir.

Figure 15 High resolution radar image of simulated scene of 20 km x 20 km, flight altitude of 8 km. Radar antenna size: 3.6 m cross track x 4.4 m along track.
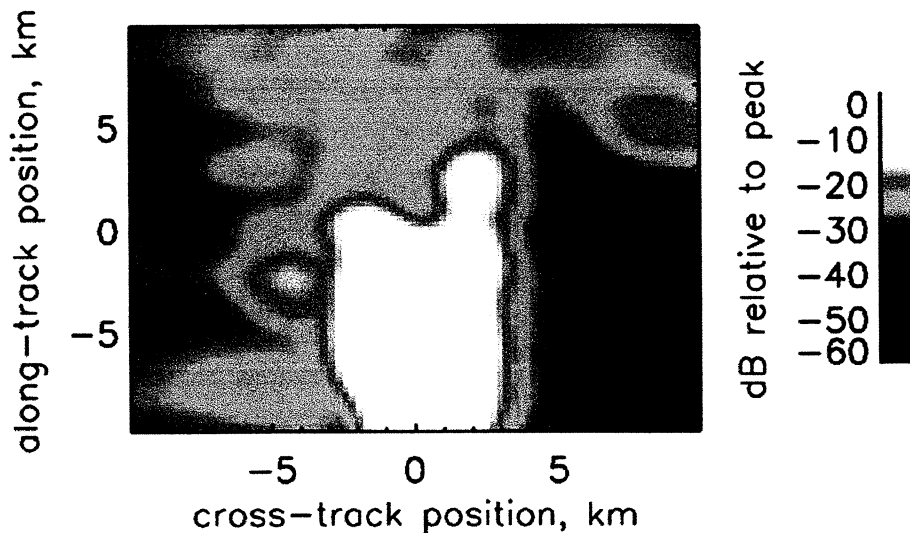
Figure 16. Low resolution radar image of simulated scene of 20 km x 20 km, flight altitude of 8 km. Radar antenna size: .93 m cross track, .93 m along-track.

7. Implementing the Radar Beamforming Algorithm

Pulsed Radar with Digital Receiver

The N-channel digitizer/signal processor card is shown in Figure 7. The digital tuner (Graychip GC1012A, shown in Figure 17) has a user selectable digital local oscillator, allowing any center frequency to be selected between 0 and Fs/2, where Fs is the clock frequency. The nominal center frequency will be 20 MHz. This is followed by a digital decimation filter (low pass) that limits the bandwidth of the I and Q output, and also increases the dynamic range of the signal. The GC1012A currently runs at 80 MHz, but there is a planned upgrade to 100 MHz with the GC1012B.
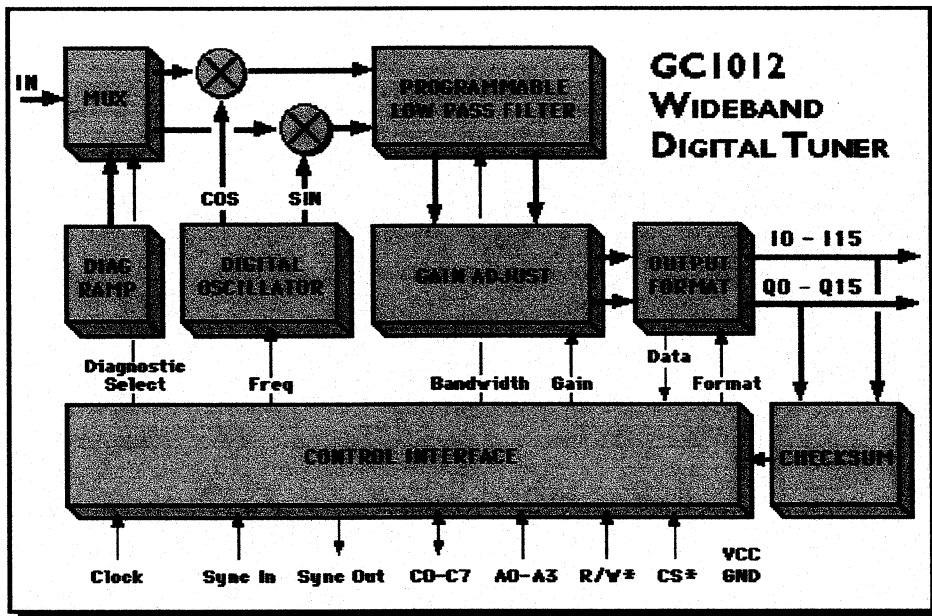

Figure 17 Graychip GC1012A digital tuner block diagram.

Case 2 Beamforming Algorithm in the FPGA

We begin with Case 2 beamforming, since it is the easiest to describe. In-phase (I) and Quadrature (Q) pairs as a function of time for each of N receivers will be formatted $I(U,V,W)$, $Q(U,V,W)$ where U is the receiver number, V is the sample vector number, and W is the range gate number. A sample vector of Ng range gates occurs every time the radar is triggered. A timing trigger from the radar control card will be sent to the FPGA to determine the timing of the first gate. The number of gates, Ng, should be programmable. Data will arrive from each receiver as shown in Table 3.

Before further processing, the raw I and Q data need to be scaled by a complex constant, A_i particular to each receiver. This scaling accounts for any amplitude and phase imbalance between the receivers, and is also used to add an amplitude taper to the received voltages to reduce sidelobe levels. Let

$$A_i = I_i + jQ_i$$

then the corrected I and Q values, I_c and Q_c, are given by

$$I_c = I \cdot I_i - Q \cdot Q_i \quad \text{and} \quad Q_c = Q \cdot I_i + I \cdot Q_i .$$

Table 4 shows the data format at the input to the beamforming algorithm for sample vector 1. There is no latency required to execute the beamforming algorithm, thus computation of the algorithm can begin as soon as the samples arrive for range gate 1 for all of the receivers. The data in

Table 4 will be processed into instantaneous beam powers, $P(\theta_m, V, W)$, using the following formula

$$P(\theta_m,V,W) = \left[\sum_{i=0}^{N-1} I_c(i,V,W)\cos(ikd\sin\theta_m) - Q_c(i,V,W)\sin(ikd\sin\theta_m) \right]^2 +$$

$$\left[\sum_{i=0}^{N-1} Q_c(i,V,W)\cos(ikd\sin\theta_m) + I_c(i,V,W)\sin(ikd\sin\theta_m) \right]^2$$

where $k = 2\pi/\lambda$, d is the spacing between the N subarrays, and θ_m is the scan angle of the mth beam peak measured from broadside.

Table 3. Data format for each receiver channel in the array, shown for receiver 1.

	Gate 1	Gate 2	....	Gate Ng
Sample vector 1	I(1,1,1),Q(1,1,1)	I(1,1,2),Q(1,1,2)		I(1,1,Ng),Q(1,1,Ng)
Sample vector 2	I(1,2,1),Q(1,2,1)			
Sample vector 3	I(1,3,1),Q(1,3,1)			
....				
Sample vector Ns	I(1,Ns,1),Q(1,Ns,1)			I(1,Ns,Ng),Q(1,Ns,Ng)

Table 4. Data format at input to beamforming algorithm.

	Gate 1	Gate 2	...	Gate Ng
Receiver 0	$I_c(0,1,1),Q_c(0,1,1)$	$I_c(0,1,2),Q_c(0,1,2)$		$I_c(0,1,Ng),Q_c(0,1,Ng)$
Receiver 1	$I_c(1,1,1),Q_c(1,1,1)$			
Receiver 2	$I_c(2,1,1),Q_c(2,1,1)$			
...				
Receiver N-1	$I_c(N-1,1,1),$ $Q_c(N-1,1,1)$			$I_c(N-1,1,Ng),$ $Q_c(N-1,1,Ng)$

Case 1 beamforming algorithm in the FPGA

In-phase (I) and Quadrature (Q) pairs as a function of time for each of N receivers will be formatted $I(M,U,V,W)$, $Q(M,U,V,W)$ where M is the transmit beam number, U is the

receiver number, V is the sample vector number, and W is the gate number. Table 5 shows the data format at the input to the beamforming algorithm for sample vector 1. The data in Table 5 will be processed into instantaneous beam powers, $P(\theta_m, V, W)$, using the following formula

$$P(\theta_m, V, W) = \left[\sum_{i=0}^{N-1} I_c(m, i, V, W) \cos(ikd \sin \theta_m) - Q_c(m, i, V, W) \sin(ikd \sin \theta_m) \right]^2 +$$

$$\left[\sum_{i=0}^{N-1} Q_c(m, i, V, W) \cos(ikd \sin \theta_m) + I_c(m, i, V, W) \sin(ikd \sin \theta_m) \right]^2 .$$

Table 5. Data format at input to beamforming algorithm (Case 1 beamforming).

	Gate 1	Gate 2	.	Gate Ng
Receiver 0	$I_c(1,0,1,1), Q_c(1,0,1,1)$	$I_c(1,0,1,2), Q_c(1,0,1,2)$		$I_c(1,0,1,Ng), Q_c(1,0,1,Ng)$
Receiver 1	$I_c(1,1,1,1), Q_c(1,1,1,1)$			
Receiver 2	$I_c(1,2,1,1), Q_c(1,2,1,1)$			
...				
Receiver N-1	$I_c(1,N-1,1,1),$ $Q_c(1,N-1,1,1)$			$I_c(1,N-1,1,Ng),$ $Q_c(1,N-1,1,Ng)$

For Case 1 and Case 2 beamforming, the final output product, $P_{ave}(\theta_m, W)$, will be averaged over several sample vectors as

$$P_{ave}(\theta_m, W) = \sum_{V=1}^{N_s} P(\theta_m, V, W) .$$

This final vector provides a matrix of the average beam power as a function of beam position and range gate.

Typical values for the various parameters for airborne and space-based systems are summarized in
Table **6**. The number of vectors per second was computed for the airborne system assuming that a full set of beams were generated every half antenna diameter along track. This was also the basis for the spaceborne system, Case 2 beamforming. For the

spaceborne system with Case 1 beamforming, the rate was based on the assumption of 10 independent samples (looks) per 10 km x 10 km pixel.

Table 6. Summary of key parameters for airborne and spaceborne radar configurations.

Parameter	Airborne radar	Spaceborne radar
Number of receivers	10	120
Number of range gates, Ng	20	240
Number of sample vectors per averaging period, Ns	10-100	10-100
Number of beams	20	240
Number of sample vectors per second, Case 1 beamforming	5200	3600
Number of sample vectors per second, Case 2 beamforming	260	2000

If a single signal processing board or ASIC is unable to handle this processing load, the algorithm can be partitioned in a number of ways. To minimize the number of input lines to the processor, the algorithm can be partitioned among groups of receivers. If this is done, the calculation of $P(\theta_m, V, W)$ must be modified. Partial sums for the kth processor can be computed as follows:

$$V_{\text{Re}}(k, \theta_m, V, W) = \left[\sum_{i=0}^{N-1} I_c(m, i, V, W) \cos(ikd \sin \theta_m) - Q_c(m, i, V, W) \sin(ikd \sin \theta_m) \right]$$

$$V_{\text{Im}}(k, \theta_m, V, W) = \left[\sum_{i=0}^{N-1} Q_c(m, i, V, W) \cos(ikd \sin \theta_m) + I_c(m, i, V, W) \sin(ikd \sin \theta_m) \right]$$

Where $V_{\text{Re}}(k, \theta_m, V, W)$ and $V_{\text{Im}}(k, \theta_m, V, W)$ are the real and imaginary parts of the partial sum. These partial sums can be combined off-line:

$$P(\theta_m, V, W) = \left[\sum_{k=0}^{N_p-1} V_{\text{Re}}(k, \theta_m, V, W) \right]^2 + \left[\sum_{k=0}^{N_p-1} V_{\text{Im}}(k, \theta_m, V, W) \right]^2$$

where N_p is the number of processors.

8. Cost analysis

A cost breakdown for the radar is attached as an Excel spreadsheet. This cost analysis was carried out for ten t/r units.

Component	Vendor	Part No.	Price/Unit	Quantity	Total
Ultra-STALO	Miteq	XTO-05-20-J-15P	$1,000	1	$1,000.00
1.26 GHz PLO	Miteq	CP-1260-15P	$1,000	1	$1,000.00
1.24 GHz PLO	Miteq	CP-1240-15P	$1,000	1	$1,000.00
Modulator	Pasternack	PE7112	$558	2	$1,116.00
SSPA	CTT	APM/020-3344	$1,460	10	$14,600.00
LNA	Miteq (0.9 dB)	JS2-001000200-09-10A	$695	10	$6,950.00
SPDT Switch	Pasternack	PE7112	$558	28	$15,624.00
SPST Switch	Pasternack	PE7105	$500	18	$9,000.00
Band Pass Filter	TTE	315P	$289	10	$2,890.00
Phase Shifters	ADC	ACPS-A652	$2,800	10	$28,000.00
D. Attenuators	Weinschel	ZFA-2000	$531	10	$5,310.00
Fixed attenuators	Sickles	3T (40dB)	$58	10	$580.00
8-W Power Divider	Mini-Circuits	ZB8PD-2	$140	2	$280.00
Circulator	Narda-West	CNA1214	$273	10	$2,730.00
Directional Couplers	Narda-East	4042-20	$306	10	$3,060.00
Mixers	Miteq	DM0052LA2	$365	10	$3,650.00
IF Amplifiers	Miteq	AU-1337	$285	10	$2,850.00
IF Band Pass Filters	Allen Avionics		$267	10	$2,670.00
Power Supplies	Acopian		$5,000	1	$5,000.00
Cables/connectors					
Semi-flex	Tensolite		$2,500	1	$2,500.00
Hardware	Various Vendors		$2,500	1	$2,500.00
Temperature Control					
Heaters/Thermistors	Minco		$35	40	$1,400.00
Control Card	ProSensing		$1,000	1	$1,000.00
Hardware/Software			$1,000	1	$1,000.00

Total   **$115,710**